Received 24 November 2025; revised 21 January 2026; accepted 7 April 2026. Date of publication 13 April 2026; date of current version 15 April 2026.

Digital Object Identifier 10.1109/OJCOMS.2026.3683151

Exploiting Angular Diversity for Passive Positioning VLC Systems

ALEJANDRO LÓPEZ BARRIOS (Student Member, IEEE), BORJA GENOVÉS GUZMÁN (Senior Member, IEEE), AND MÁXIMO MORALES-CÉSPEDES (Member, IEEE)

Departmento de Teoría de la Señal y Comunicaciones, Universidad Carlos III de Madrid, Leganés 28911, Spain

CORRESPONDING AUTHOR: A. L. BARRIOS (alelopez@pa.uc3m.es)

This work was supported in part by the Project SOFIA-AIR funded by MCIN/AEI/10.13039/501100011033/ERDF, UE, under Grant PID2023-147305OB-C31; in part by the Project HOLIFI6G funded by MICIU/AEI/10.13039/501100011033/FEDER, UE, under Grant PID2024-156038OA-I00; and in part by TUCAN6-CM, funded by CM (ORDEN 5696/2024) under Grant TEC-2024/COM460. The work of Borja Genovés Guzmán was supported by the Ramón y Cajal Grant funded by MICIU/AEI/10.13039/501100011033 and FSE+ under Grant RYC2022-036053-I. The work of Máximo Morales-Céspedes was supported by the Ramón y Cajal Grant funded by MICIU/AEI/10.13039/501100011033 and FSE+ under Grant RYC2023-042518-I.

ABSTRACT Retroreflective visible light communications (R-VLC) have been recently proposed for providing ultra-low power positioning and communications in the framework of the Internet of Things. Specifically, devices equipped with a corner-cube retroreflector send optical signal back to the source of light through a parallel path, where the photodetector (PD) is co-located. To obtain positioning through trilateration methods, previous works consider a large separation among PDs so that they provide at least three linearly independent channel responses. In this work, we propose a R-VLC system based on the deployment of PDs following an angular diversity arrangement onto the source plane. This approach achieves two goals; *i*) it enables trilateration-based positioning for small sources of light by implementing a single angle diversity receiver (ADR) and following a centralized structure and *ii*) it improves the footprint and precision of positioning accuracy, i.e., the area in which positioning is accurate, compared to traditional approaches. Simulation results show that the proposed scheme increases the positioning area 60%, ensuring a positioning accuracy of 1 cm. Moreover, it is also shown that positioning performance can be improved increasing the number of PDs and carefully selecting them to avoid correlated channel responses.

INDEX TERMS Visible light communication, angle diversity receiver, photodetector design, field-of-view.

I. INTRODUCTION

VISIBLE light communication (VLC) has emerged as a complementary technology to traditional radiofrequency (RF) technologies. While RF systems suffer from a congested spectrum, optical wavelengths are still untapped, offering a pervasive deployment of light-emitting diodes (LEDs) that can be exploited to provide a networked system [1]. The small and confined coverage footprint generated by each optical cell allows for large resource reuse, provides robustness against interference, and creates a grid of transmitters that leads to a smooth fair connectivity. In this sense, VLC can contribute greatly to traditional RF systems by enabling high-precision positioning in indoor scenarios [2], [3].

VLC systems are typically formulated from a downlink perspective, while the uplink design is still an open issue. Some works have considered traditional RF to perform as uplink in VLC systems, e.g., WiFi [4] and cellular networks [5]. However, the power consumption of these technologies is large [6], which prevents them from operating on the Internet of Things (IoT) networks. Recently, passive transmitters have been considered to enable low-power uplink for energy constrained IoT systems, getting rid of power-hungry active elements.

Traditional RF backscatter modulates the signals around the propagation environment by means of changing some of the receiver characteristics. For instance, an antenna can absorb and reflect such signal by modulating the matching impedance of the antenna in the IoT device. As a consequence, it is possible to get rid of any elements such as the synthesizer, which allows to save energy or even operating battery-free [7]. However, RF backscatter presents some limitations; *i*) the IoT device must be placed close to the carrier wave generator, which does not typically occur

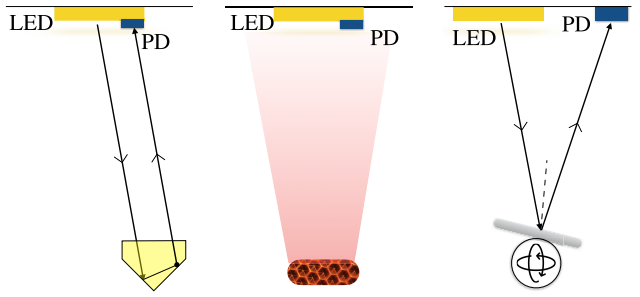

(a) Corner-cube retroreflector. (b) Retroreflective sheeting. (c) Adjustable mirror.

FIGURE 1. Elements that perform as reflectors in optical backscatter.

in practical scenarios and *ii*) it may prove inefficient in terms of spectral efficiency since the transmitted bandwidth is duplicated, which may also lead to interference.

To solve these issues and leverage the pervasive deployment of light sources, optical backscatter has recently been proposed to provide both positioning and communications. Basically, the light that impinges onto the reflecting material is modulated by means of amplitude changes or light deviation. Three main elements can perform as reflectors as shown in Fig. 1. Corner cube retroreflectors (CCRs) [8] and retroreflective sheeting [9], [10] [11], both based on reflecting the light back in the same direction as it is received, and mirrors, which allow us to reconfigure the direction of the light [12], [13]. The two first elements rely on liquid crystal (LC) shutters for modulating the light by allowing or blocking the retroreflected channel, while mirrors manage the incidence light applying tilting mechanisms that redirects it to the desired destination.

Mirror-based VLC requires knowledge about the position of the receiver to which the light must be forwarded. At this point, note that the retroreflectors generate a beam in the same direction as the incidence beam transmitted from the source of light. Therefore, retroreflective VLC (R-VLC) simply requires users located within the coverage footprint generated by each source of light. Retroreflective sheeting, e.g., the retroreflectors widely used in road safety, achieves a poor performance because they are subject to high scattering effects leading to a weak retroreflected beam. Differently, CCRs concentrate more light into the point where the source is located, achieving larger signal received power. In [14], the performance of multiple retroreflectors is experimentally compared, and it confirms that the CCRs obtain better communication performance than other retroreflective structures.

In this context, few prior works have considered CCRs to exploit the retroreflected optical channel for both communications and positioning. In [15] and [16], the closed-form expressions for the retroreflected channel model, assuming that the receiver of the retroreflected signal is much smaller than the CCR, are derived following a geometrical analysis. After that, these works analyze the obtained channel model for positioning applications achieving an accuracy below 1 cm. Lately, the potential of this approach has been shown in real applications such as localization in mining environments [17]. These works are basically based on implementing an LC shutter to modulate the reflected optical signal. Then, each retroreflector generates an uplink channel in which a tag is transmitted. In this sense, the uplink interference due to transmission of different can be modeled similarly as a downlink VLC system. Therefore, well known techniques such as orthogonal resource allocation [18], non-orthogonal multiple access (NOMA) [19], precoding schemes [20], [21] or adding optical rotatory dispersor [15] can be potentially applied to avoid or minimize the impact of the interference.

Focusing on the positioning performance, notice that at least three linearly independent channel responses are required to compose a trilateration equation system. However, the signals received by close PDs pointing to the same direction can be extremely correlated because of the lack of small propagation effects in the optical domain. To avoid the correlation among PDs, the state-of-the-art positioning systems based on R-VLC propose the deployment of an arrangement of PDs sufficiently separated onto the source of light, e.g., [8] and [16]. As a consequence, this approach is limited to large source lights, e.g., large LED panels, to receive the backscattered optical signals.

To solve this issue, we propose the use of angle diversity receivers (ADRs). ADRs based on deploying multiple PDs following an angular arrangement have been traditionally proposed for improving the communication performance in optical MIMO systems by reducing the correlation among channel responses of adjacent users [22], [23]. In this work, beyond communications enhancement, we exploit the angular diversity offered by ADRs to improve the accuracy of positioning and enable positioning using small LEDs. It is worth remarking that exploiting the angle diversity of a large amount of PDs may lead to complex receivers. In such a way, the concept of reconfigurable photodetector, in which the set of PDs is connected to a single or a limited number of signal processing chains through a selector, is proposed to relax the receiver complexity in [24].

In this work, we propose a novel approach for providing both positioning and communications in R-VLC that combines the use of CCR in the user devices and ADRs deployed onto the light source plane of LED fixtures. The CCR enhances the ability to detect and locate users by reflecting light back to its source, while the ADR allows the system to sense the reflected light from multiple angles, improving positioning accuracy and reducing the required size of the light source. This model can be extended to perform as a dual-purpose system, enabling simultaneous data communication and positioning, making it an ideal solution for a wide range of IoT applications. The main contributions of this work can be summarized as follows:

1) The effective retroreflected area (ERA) that determines the optical power that is retroreflected by the CCR and, then, captured by the PDs deployed onto the source of light, is derived considering that they follow an angular diversity arrangement.

2) A decentralized ADR approach is proposed to minimize the shadow generated by the PDs in the optical beam received and retroreflected by the CCR. The geometrical constraints of this approach are derived. After that, theoretical and simulated ERA values are computed to validate the proposed scheme based on retroreflection to ADRs.
3) Once the ERA and power received by each PD of the ADR are determined, the positioning methodology is formulated. The exceed of degrees of freedom due to the angular diversity provided by the ADR enables to derive PD selection methods. Interestingly, it is shown that for ADRs composed of a large number of PDs, maximizing the channel variation subject to a power threshold achieves better results than selecting PDs providing the strongest received signal because of the correlation among close PDs.

Simulation results show that the proposed scheme enables a good positioning accuracy, even when deployed in small LEDs, avoiding the need for large LED panels. Moreover, assuming the same number of PDs as in the non-angular approach, the proposed scheme based on angular diversity increases the positioning footprint area by 60%. It is also shown that increasing the number of PDs requires managing the channel correlation to increase the positioning performance. Since the proposed approach enables the use of ADRs for communication purposes, the inherent enhancement of the communication rate because of exploiting the angular diversity is also briefly analyzed.

The remainder of this paper is organized as follows. In Section II the R-VLC system model is presented. Section III presents the impact of ADR in the signal retroreflected by the CCR. The methodology for obtaining positioning is presented in Section IV. Specifically, two methods named highest-power and highest-variation are derived. The communications performance is briefly presented in Section V. Simulation results are presented in Section VI. Finally, Section VII provides concluding remarks.

II. SYSTEM MODEL

We consider an indoor VLC system where a single light source based on LED panel technology illuminates the room in which K, $k = \{1, \ldots, K\}$, users are located. The spatial dimensions of the room are modeled as a 3D Cartesian coordinates $\left[x\ y\ z\right]$ system as described in Fig. 2. The LED is pointing perpendicularly to the floor according to the unitary vector $\hat{\mathbf{n}} = \left[0\ 0\ -1\right]$. Besides, on the surface of the LED panel, an ADR composed of I, $i = \{1, \ldots, I\}$, PDs is integrated for which the PD i is characterized by the normal pointing vector denoted by $\mathbf{v}_i$ and position vector $\mathbf{q}_i$. The distance between the center of the LED panel and the user k is given by $d_k = \|\mathbf{u}_k - \mathbf{r}\|$, where $\mathbf{u}_k$ is the position vector containing the coordinates of the user k, i.e., $\mathbf{u}_k = \left[d_x\ d_y\ d_z\right]$ and $\mathbf{r}$ is the position vector of the LED. Each user is equipped with a CCR, so that the optical signal that falls on the user is returned to the source following the same propagation path.

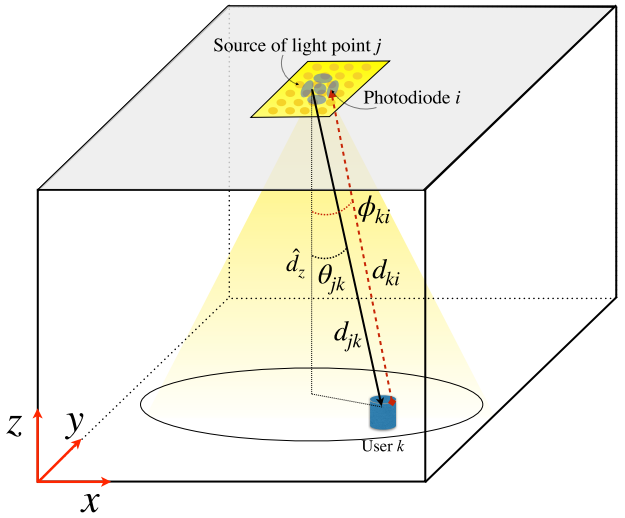

FIGURE 2. Indoor R-VLC scenario based on CCR.

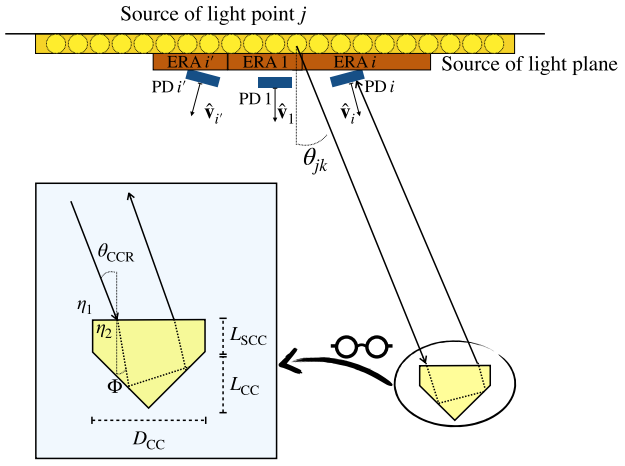

FIGURE 3. Geometry of the optical retroreflection based on CCR.

Notice that this approach transforms the user into a passive target. As a consequence, the retroreflected rays of light can be detected by the PDs deployed along the LED panel following an angular diversity arrangement for subsequent signal processing.

The geometry of the CCR is characterized by its length, recession length, and diameter of the front facet, denoted by L_{CC}, L_{SCC}, and D_{CC}, respectively. The shape of the retroreflector face is called the input aperture, while the outline of the retroreflected beam is referred to as the output aperture. The composition of a CCR is described in Fig. 3. The shape and dimension of the CCR determine the input and output aperture regions, which correspond to the regions formed by all the light rays that enter and the reflected rays, respectively. Moreover, their intersection generates the ERA on the CCR plane. Based on the geometrical derivation from previous studies [8], [16], the output apertures offsets because of both CCR and recession lengths are given by

$$D = 2L_{CC}\tan(\Phi) \tag{1}$$

and

$$D_s = 2L_{SCC}\tan(\Phi), \tag{2}$$

respectively, where Φ represents the refraction angle, which is determined by the refraction index of the material of the CCR denoted by η and the angle of incidence of the light striking it denoted by θ_{CCR}. Then, according to Snell's law,

$$\Phi = \arcsin\left(\frac{\eta_1 \sin\theta_{CCR}}{\eta_2}\right), \tag{3}$$

where η_1 and η_2 are the refractive index of the media on either side of the interface. It is worth remarking that the equations described above characterize the retroreflection of the light at the CCR and, ultimately, they determine the resulting ERA.

This work adopts the retroreflected signal model proposed in [8] and [16]. Specifically, the signal retroreflected from user k and received at PD i deployed at the source of light is

$$y_{ik} = \rho_i \beta h_{ik} x + z_i, \tag{4}$$

where ρ_i represents the responsivity of the PD, $\beta \in [0,1]$ is the reflecting loss factor, h_{ik} is the channel between the PD i deployed on the source of light and the signal retroreflected by the CCR of user k, and z_i is the additive white Gaussian noise (AWGN). Unlike prior works, we cannot consider the light source as a single point because we assume the deployment of a realistic LED panel with dimensions comparable to the size of the room. To characterize the optical propagation from an LED panel, it is assumed that the source of light is composed of J, $j = \{1,\ldots,J\}$, points uniformly distributed transmitting the same optical power each. Moreover, the ratio of the ERA employing a CCR is denoted by $\epsilon \in [0,1]$. Following this approach, the channel between the transmitted and the received signal at PD i coming from the CCR at user k can be written as

$$h_{ik} = \begin{cases} \dfrac{\epsilon}{J}\displaystyle\sum_{j=1}^{J} \dfrac{A_i(m+1)}{2\pi\left(d_{jk}+d_{ki}\right)^2}\cos^m\left(\theta_{jk}\right)\cos\left(\phi_{ki}\right) & \phi_{ki} \le \psi_i \\ 0 & \phi_{ki} > \psi_i \end{cases} \tag{5}$$

where A_i is the effective area of PD i, m is the Lambertian emission index, d_{jk} is the distance from the point of light j to the CCR of user k, and d_{ki} is the distance from user k to PD i of the ADR deployed on the LED panel. Moreover, in (5), ψ_i is the field-of-view (FoV) of the PD, and the radiation and incidence angles are denoted by θ_{jk} and ϕ_{ki}, respectively. The Lambertian emission order is defined as $m = \frac{-1}{\log_2\left(\cos\theta_{\frac{1}{2}}\right)}$, where $\theta_{\frac{1}{2}}$ is the transmitter semi-angle at half-power. We assume circular PDs with an area $A_i = \frac{\pi}{4}D_{PD}^2$, where D_{PD} represents the diameter of the PD.

This proposal can be easily scaled to a multi-LED architecture producing a single-input multiple-output (SIMO) system in the uplink, where the signal is received by PDs co-located with multiple light sources from which the light is emitted and that impinges onto the user device. This would increase reliability of the system and a better positioning accuracy. For simplicity, we focus on a single light source architecture.

III. IMPACT OF ADRS IN THE RETROREFLECTIVE AREA

The ERA corresponds to the area of the LED panel whose transmitted light is retroreflected by the CCR and collected by the set of PDs deployed on the light source plane as described in Fig. 3. In [16], the authors determine the ERA as a function of input and output apertures because of the incidence angle and the recession of the CCR assuming that the front face of the retroreflector is much larger than the PD area. This approach is extended in [8] for the cases in which the area of PDs is larger than or similar to the aperture of the front face of the retroreflector. However, both works assume that the PDs on the light source plane are pointing perpendicularly downwards to the floor.

At this point, notice that solving a linear equation system or determining the position from the signals received at multiple PDs depends on how different are the channel responses to obtain these signals. For instance, if two locations are subject to the same or very similar channel, it results more difficult to distinguish both than if they correspond to different or dissimilar channel responses. To measure the similarity between channel responses, we propose to calculate the correlation between the channel of two positions as [23] and [25]. Specifically, considering the set of vector pairs $\left(\mathbf{h}_p, \mathbf{h}_q\right)$, $p,q = 1,\ldots,N : p \neq q$, assuming that each pair (p,q) is counted only once, where N is the number of possible vector combinations considering a specific number of PDs (typically 3 for determining the position), the channel correlation coefficient is defined as

$$\Gamma_\Sigma = \frac{1}{N}\sum_{n=1}^{N} \underbrace{\frac{\mathbf{h}_p \cdot \mathbf{h}_q}{\sqrt{\left(\mathbf{h}_p \cdot \mathbf{h}_p\right)\left(\mathbf{h}_q \cdot \mathbf{h}_q\right)}}}_{\gamma\left(\mathbf{h}_p,\mathbf{h}_q\right)}, \forall p,q \in \{1,\ldots,K\}, p \neq q, \tag{6}$$

where, in this case, $\gamma\left(\mathbf{h}_p, \mathbf{h}_q\right)$ corresponds to the correlation coefficient between two positions p and q. That is, the correlation coefficient in (6) measures the similarity between channel responses of two positions for all possible PDs combinations.

For illustrative purposes, let us consider an scenario composed of 2 PDs separated a distance S_{PD} between them and subject to an elevation angle γ as depicted in Fig. 4(a). User 1 is in a fixed position at the center of the one-dimensional scenario, while user 2 is in a movable position along the scenario. The correlation coefficient between the channel of both positions is depicted in Fig. 4(b) considering exclusively the separation between PDs and also the angular diversity given by an elevation equal to 10° and 45°. For a short distance between PDs, it can be seen that the channel responses between both positions are highly correlated in

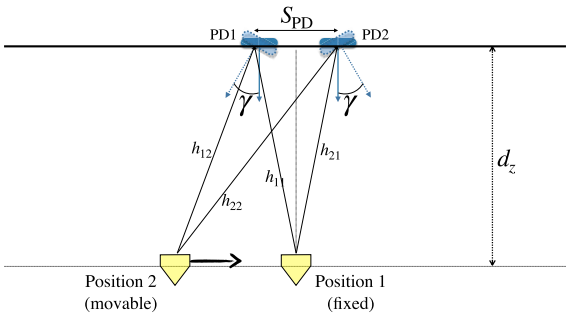

(a) Toy example scenario.

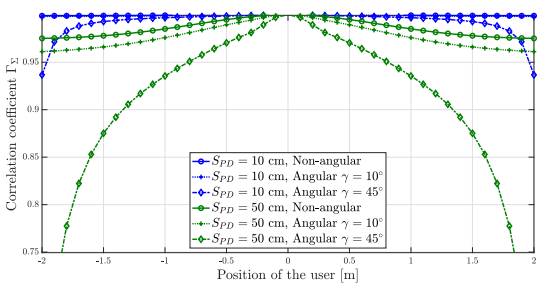

(b) Correlation coefficient vs. position of the movable user.

FIGURE 4. Toy example for evaluating the correlation between channel responses at adjacent positions.

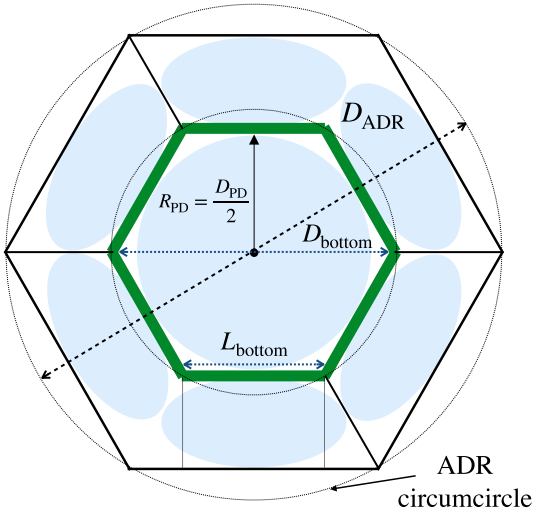

(a) Plan of the centralized pyramidal ADR.

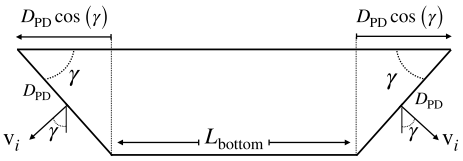

(b) Profile of the centralized pyramidal ADR.

FIGURE 5. Architecture of the centralized pyramidal ADR.

the entire distance range. In fact, considering angle diversity by adding an elevation angle of only 10° leads to similar results. In this sense, an elevation angle of 45° reduces the correlation significantly in comparison with the non-angular approach. On the other hand, for a distance between PDs equal to 50 cm, it can be seen that the correlation coefficient decreases. For $S_{\text{PD}} = 50$ cm, it is also shown that combining both approaches; distance separation and angle diversity, leads to a considerable reduction of the correlation.

Previous positioning R-VLC works are based on managing the similarity among channel responses by only separating the PDs following a non-angular approach, e.g., [8] and [16]. Notice that this constraint involves the following issues:

- In contrast to RF propagation, optical signal is not subject to small scale effects. Besides, previous works for positioning in R-VLC do not consider angular diversity, while the PDs are separated a specific distance among them. As a consequence, the signal received at adjacent points can be extremely correlated. As described in Fig. 4a, a considerable distance among PDs is required to avoid high correlation among their channel responses. Therefore, previous positioning schemes may not be applied for small sources of light such as small LED panels.
- The output aperture offsets because of the structure of the CCR lead to a coverage footprint in which the R-VLC system provides accurate positioning. Considering PDs pointing downwards to the floor, i.e., without angular diversity, a fixed, small and confined positioning footprint is generated.

For simplicity, a pyramidal arrangement is proposed for the ADR design. Specifically, we assume an odd number of PDs so that the first value of index i corresponds to a PD pointing perpendicularly to the floor. That is, $\mathbf{v}_1 = \begin{bmatrix}0 & 0 & -1\end{bmatrix}$. Then, denoting the elevation and azimuthal angles by $\gamma \in \left[0, \frac{\pi}{2}\right]$ and $\delta \in [0, 2\pi)$, respectively, the pointing vector of PD i is given by

$$\mathbf{v}_i = \begin{bmatrix}\sin(\gamma_i)\cos(\delta_i) & \sin(\gamma_i)\sin(\delta_i) & -\cos(\gamma_i)\end{bmatrix}, \tag{7}$$

where, for the pyramidal arrangement,

$$\delta_i = \frac{(i-1)2\pi}{I-1}, \quad i = 2, \ldots, I \tag{8}$$

and

$$\gamma_i = \gamma_{\text{pyr}}, \quad i = 2, \ldots, I, \tag{9}$$

where γ_{pyr} is the elevation of the facets of the pyramid. It is worth remarking that other arrangements, e.g., hemispherical or multi-tier, can be considered and their application is straightforward. Notice also that the pyramidal configuration does not involve the construction of pyramidal structure. That is, the PDs can be distributed satisfying (8) and (9) along the LED panel. Moreover, it is assumed that each PD occupies the inscribed circle of each facet of the pyramidal structure, i.e., the circle tangential to the sides of the facet. Therefore, the distance from the center point of the pyramid vertex to the center point of one of its facets is denoted by $R_{\text{PD}} = \frac{D_{\text{PD}}}{2}$ as described in Fig. 5. This value is computed as $R_{\text{PD}} = \frac{L_{\text{bottom}}}{2\sin\frac{\pi}{I-1}}$,

where L_{bottom} is the side of the polygon that truncates the pyramid.

At this point, the concept of ERA described in previous works still results valid for ADR configurations deployed onto the light source plane.[1] However, for the proposed approach, the ERA directly depends on the structure of the ADR. Specifically, the following two approaches are considered.

A. CENTRALIZED ADR CONFIGURATION

Traditionally, the concept of ADR is based on a compact structure in which the set of PDs are deployed on a geometrical composition. It is assumed that the light does not pass through this structure. Let us consider a truncated pyramid model and circular PDs as described in Fig. 5. The PD $i = 1$, which points downwards to the floor, fits in the shape of a regular polygon, as highlighted in green in Fig. 5, with apothem $a_{\text{bottom}} = \frac{D_{\text{PD}}}{2}$. Therefore, the circle that passes through all the vertices of the polygon is given by a diameter $D_{\text{bottom}} = \frac{L_{\text{bottom}}}{\sin\left(\frac{\pi}{I-1}\right)}$. Since the side of a regular polygon can be written as a function of the apothem as $L_{\text{bottom}} = 2\ a_{\text{bottom}} \tan\left(\frac{\pi}{I-1}\right)$, where a_{bottom} denotes the apothem, the radius of the circumcircle of the bottom face of the ADR is $R = \frac{D_{\text{PD}}}{2\cos\left(\frac{\pi}{I-1}\right)}$. Then, considering 2 opposite facets of the pyramid, the circle that circumvents the top base of the pyramid is given by a diameter equal to

$$D_{\text{ADR}} = D_{\text{PD}} \left(\frac{1}{2\cos\left(\frac{\pi}{I-1}\right)} + 2\cos(\gamma) \right). \tag{10}$$

Therefore, the ERA can be approximated[2] similarly as in [8] considering the area occupied by the ADR as a single PD. For this case, the ratio between the ERA and its maximum is a weight factor on the retroreflected channel given by

$$\begin{aligned} \varepsilon &= \frac{A_{\text{ERA}}}{A_{\text{ERA}_{\max}}} \\ &= \frac{2\xi^2 \left(\cos^{-1}\left(\frac{\Delta_D}{\xi}\right) - \frac{\Delta_D}{\xi} \sin\left(\cos^{-1}\left(\frac{\Delta_D}{\xi}\right)\right)\right) - \frac{\pi}{4} D_{\text{ADR}}^2}{\pi\xi^2 - \frac{\pi}{4} D_{\text{ADR}}^2} \end{aligned} \tag{11}$$

where $\Delta_D = D + D_S$ and $\xi = D_{\text{CC}} + \frac{D_{\text{PD}}}{2}$.

B. DECENTRALIZED ADR CONFIGURATION

At this point, recall that the ERA corresponds to the area retroreflected by the CCR, which, after that, is collected by the PDs. As a consequence, for the centralized configuration, it can be seen that the signal retroreflected along the aperture of the CCR is not only blocked by the corresponding PD, but also by the adjacent PDs that compose the centralized ADR, which may penalize the total amount of the retroreflected signal. At this point, we propose a decentralized ADR structure in which the distance among PDs satisfies a minimum distance ensuring that the ERAs received at any two different PDs do not overlap between them. Notice that each PD occupies its projection onto the light source plane. According to [8], the diameter of the light emitting surface that contributes to the retroreflection is $D_{\text{PD}} + 2D_{\text{CC}}$, i.e., the diameter of $A_{\text{ERA}_{\max}}$. Therefore, to maximize the ERA generated around the set of PDs that compose the ADR, the minimum separation among them must satisfy the following condition

$$S_{\text{PD}} > \frac{D_{\text{PD}} + 2D_{\text{CC}}}{2}. \tag{12}$$

The proposed approach allows obtaining a greater amount of retroreflected light in each PD than the centralized ADR configuration since only a single PD may block the light that is retroreflected by the CCR. The area occupied by each PD along the light source area is reduced because of the elevation angle, as can be seen in Fig. 6. Applying the Monge method, the projection of a circular PD with area A_i onto the light source plane corresponds to an ellipse with area $A_i \cos\gamma$. Therefore, the ratio between the maximum and the obtained ERA for PD i can be written as

$$\begin{aligned} &\varepsilon_i \\ &= \frac{2\xi^2 \left(\cos^{-1}\left(\frac{\Delta_D}{\xi}\right) - \frac{\Delta_D}{\xi} \sin\left(\cos^{-1}\left(\frac{\Delta_D}{\xi}\right)\right)\right) - A_i \cos(\gamma)}{\pi\xi^2 - A_i \cos(\gamma)}. \end{aligned} \tag{13}$$

For the sake of clarity, let us define $A_{\text{illum}} = \pi \left(\frac{D_{\text{PD}} + 2D_{\text{CC}}}{2}\right)^2$ as the area surrounding the PDs that contributes to retroreflection and A_{LED} as the total area required for the LED. For illustrative purposes, the ERA, which is the region comprised of the J points of light that contribute to the retroreflection, is depicted in Fig. 7 for an ADR composed of 5 PDs satisfying

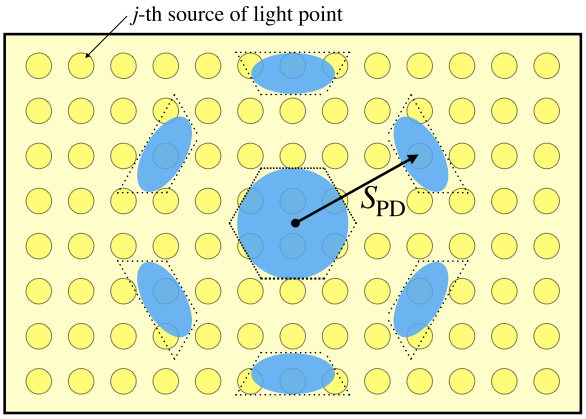

FIGURE 6. Architecture of the decentralized pyramidal ADR.

[1]The area of a PD can be considered negligible in comparison with the illumination area of an LED panel. For instance, the area of a common PD such as BPW21 corresponds to the 0.095% of the illumination area for an LED with 10 cm diameter. Considering an ADR with 5 PDs and an elevation angle of 40°, the ADR would occupy less than 0.5% of the illumination area. This percentage of occupied area would be even smaller for larger LED panels.

[2]The error because of considering the area of a regular polygon as a circle is given by $R^2\left(\pi - \frac{1}{2}n\sin\left(\frac{2\pi}{n}\right)\right)$, where R and n are the circumradius and sides of the polygon, respectively. This error tends to zero as the number of sides increases.

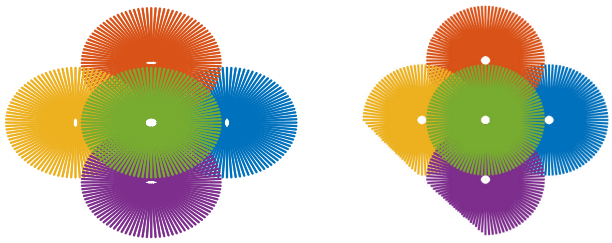

(a) User in the center of the footprint ($x = 2$ m, $y = 2$ m). (b) User located in the position ($x = 1.465$ m, $y = 1.465$ m).

FIGURE 7. Illustration of an ADR, whose PDs are separated, avoiding falling in the region of light that contributes to the retroreflection of the neighboring PD $I = 5$.

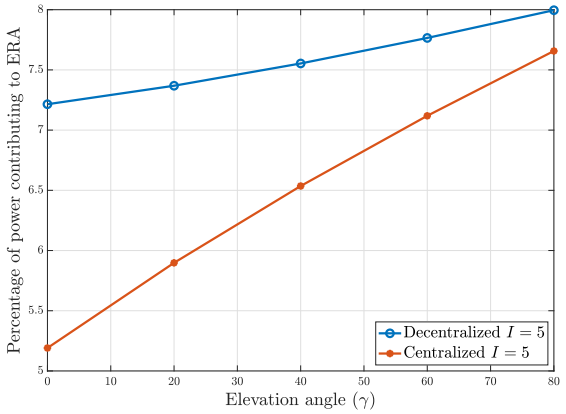

FIGURE 8. Percentage of the optical power generating ERA. 40 × 40 cm LED panel $I = 5$, $D_{CC} = 5$ cm, $L_{CC} = 3.57$ cm, $L_{CC} = 0.63$ cm, $D_{PD} = 1$ cm.

(12). Specifically, Fig. 7(a) illustrates the points assuming that the user is located in the center of the footprint, i.e., just below the LED panel. It can be seen that all the PDs generate a circular ERA around them. On the other hand, in Fig. 7(b), the user is located at the position $x = 1.465$ m, $y = 1.465$ m, and the furthest points of light disappeared, meaning that they do not contribute to the retroreflection in their corresponding PDs.

Notice that the decentralized configuration aims to increase the amount of retroreflected signal by avoiding the presence of adjacent PDs that compose the centralized ADR configuration. For instance, the white circle in the center of the ERA regions depicted in Fig. 7 corresponds to the area occupied by each PD in the decentralized configuration, whereas a larger white circle would appear for the centralized ADR configuration. For illustrative purposes, the percentage of the illumination area that is retroreflected and captured by the ADR is analyzed for both configurations in Fig. 8. It can be seen that the decentralized configuration increases the percentage of power employed for retroreflection as the elevation angle increases. Specifically, for an elevation angle of 20° the percentage of power contributing to ERA is 5.89% and 7.36% for the centralized and decentralized configurations, respectively. This difference increases with larger PD areas or smaller LED panels.

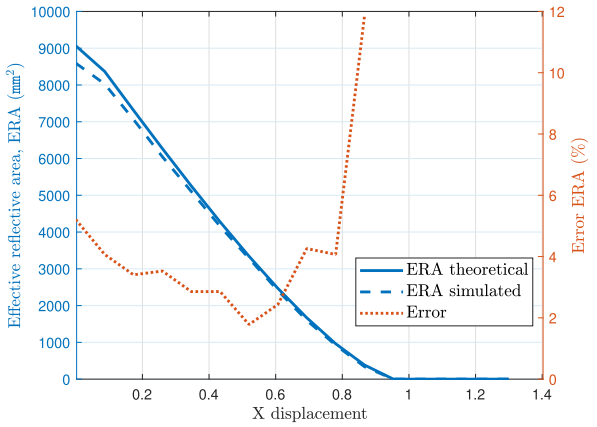

FIGURE 9. Comparison between the theoretical ERA and the simulated ERA given a rotation of the PD, $\gamma = 30°$. $D_{CC} = 5$ cm, $L_{CC} = 3.57$ cm, $L_{CC} = 0.63$ cm, $D_{PD} = 1$ cm.

The proposed ERA model is validated using the ray tracing packing available in Matlab [26]. Therefore, the ERA obtained through ray-tracing, which involves a high computational cost, can be compared with the proposed theoretical ERA in (13) for the case based on exploiting the angular diversity. The comparison between both simulation-based and theoretical ERA, and the relative error calculated as $\frac{|\text{ERA}_{\text{simulated}} - \text{ERA}_{\text{theory}}|}{\text{ERA}_{\text{simulated}}}$ are depicted in Fig. 9 as a function of the displacement between the center of the positioning footprint and the position of the user equipped with a CCR. It can be seen that both simulated and theoretical ERA follow the same shape, and the relative error is less than 10% for a displacement below 0.8 m. Notice that the error becomes greater for larger displacement values because $\text{ERA}_{\text{simulated}}$ requires a massive amount of simulated symbols for an accurate result.

IV. R-VLC POSITIONING BASED ON ADRS

The positioning system is composed of a single source of light deployed in the center of the scenario. For the sake of an easy explanation, it is assumed that interference among other sources of light or users can be avoided, e.g., considering orthogonal resource allocation schemes, so that the signal received by the PDs of the ADR is only subject to noise. The user is located in a random and unknown position and the total optical power transmitted by the LED is denoted by P_Σ. Then, the power received from the retroreflected signal at PD i of the ADR can be written as

$$P_i = \rho\beta P_t h_i + z_i, \tag{14}$$

where P_t is the transmitted optical power in the area of illumination that falls on the CCR and it is retroreflected to the source of light, which is denoted by A_{illum}. Therefore, $P_t = \frac{P_\Sigma A_{\text{illum}}}{A_{\text{LED}}}$. Besides, in (14), $z_i \sim N(0, \sigma_i^2)$, where $\sigma_i^2 = \sigma_n^2 + \sigma_{\text{interf}}^2$ corresponds to the variance because of the noise and the interference effects that are not completely avoided and, therefore, treated as noise, denoted by σ_n and σ_{interf}, respectively. Specifically, σ_n^2 is defined as the sum

of the variance of both the thermal and shot noise [27], $\sigma_n^2 = \sigma_{\text{shot}}^2 + \sigma_{\text{thermal}}^2$. The thermal noise variance is

$$\sigma_{\text{thermal}}^2 = \frac{4kT_{\text{k}}}{R_{\text{L}}}B, \tag{15}$$

where B is the modulation bandwidth, $k = 1.38 \times 10^{-23}$J/K is Boltzmann's constant, T_{k} is the absolute temperature in Kelvin, and R_{L} is the load resistance. On the other hand, the shot noise is given by,

$$\sigma_{\text{shot}}^2 = 2q\rho_i P_{\text{n}} B \tag{16}$$

where q is the electron charge, and P_{n} is the average background noise power. Note that some points of the light sources are blocked by the PD itself, so the received power is computed considering only the points of light without obstruction.

For the proposed 3D scenario, we briefly describe the geometry of the propagation path. The radiance angles from the point j of the source of light to the user and from the retroreflected light to any PD of the ADR can be determined as $\theta_j = \arccos\frac{d_z}{d_j}$. Recall that d_z is the height between the point of light and the user, and d_j is the Euclidean distance from the point of light to the user as shown in Fig. 2. Furthermore, the incidence angle at PD i in the ADR is determined by its normalized pointing vector denoted by $\mathbf{v}_i$. Then, the incidence angle is given by $\phi_i = \arccos\left(\frac{(\mathbf{u}-\mathbf{q}_i)\cdot\mathbf{v}_i}{d_i\|\mathbf{v}_i\|}\right)$. To reduce computational complexity, we approximate all distances d_j as d_i. Therefore, in the processing stage, instead of estimating J distances per PD, it estimates only one per PD. Moreover, considering that the received power is coming from an unknown position, at the processing stage, the system cannot determine which specific points of light contributed to the retroreflection. Consequently, for estimating ε we use (10) and (13) for the centralized and decentralized configuration, respectively.

The geometrical analysis described above allows us to relate the received power at each PD of the ADR with the position of the user. Let's define $\hat{\mathbf{u}} = [\hat{d}_{\text{x}}, \hat{d}_{\text{y}}, \hat{d}_{\text{z}}]$ as the estimated position vector. After some mathematical rearrangement, the predicted received power at PD i in the ADR can be expressed as

$$\hat{P}_i = \beta\rho P_{\text{t}} \text{C}\left(\frac{1}{\|\hat{\mathbf{u}}-\mathbf{q}_i\|}\right)^2\left(\frac{\hat{d}_{\text{z}}}{\|\hat{\mathbf{u}}-\mathbf{q}_i\|}\right)^m\left(\frac{(\hat{\mathbf{u}}-\mathbf{q}_i)\cdot\mathbf{v}_i}{\|\hat{\mathbf{u}}-\mathbf{q}_i\|\|\mathbf{v}_i\|}\right)\hat{\varepsilon}, \tag{17}$$

where $\text{C} = \frac{(m+1)A_i}{8\pi}$. Assuming that the geometrical parameters of the CCR are known at the processing stage, (17) presents three unknowns; $\hat{d}_{\text{x}}$, $\hat{d}_{\text{y}}$, and $\hat{d}_{\text{z}}$, which can be computed by knowing the received signal power of at least three PDs of the ADR. Notice that ADRs composed of PDs with very narrow FoVs, i.e., non-overlapping ADRs, may lead to increase the probability of not receiving a useful signal from at least three of them, while enabling to manage the interference only exploiting the angular diversity [24]. Therefore, the greater the overlap of the FoVs of the PDs, the higher the probability of finding an accurate estimated position. Note that while traditional trilateration systems use a fourth reference signal to correct timing errors and ensure precise 3D positioning, calculating a 3D position is mathematically possible with only three signals. The intersection of 3 spheres results in two possible points in space, one above and another below the ceiling. We select the latter which is the most reasonable.

At this point, recall that the goal of the proposed scheme is to estimate the position of the user based on the received power. The position is calculated solving the optimization problem given by minimizing the sum of the squared errors derived from equations (14) and (17). That is,

$$\hat{\mathbf{u}}_{\text{opt}} = \arg\min_{\hat{\mathbf{u}}} \sum_i f_i(\hat{\mathbf{u}})^2, \tag{18}$$

where

$$f_i(\hat{\mathbf{u}}) = P_i - \hat{P}_i. \tag{19}$$

The MATLAB *fsolve* solver is used to find the estimated position vector. Specifically, the Levenberg-Marquardt (LM) algorithm is applied to solve it, an iterative method frequently used in the literature on positioning in wireless communication [28], [29], [30]. By carefully selecting the initial values, the algorithm converges to a global minimum.

A. EXPLOITING THE ANGULAR DIVERSITY THROUGH PD SELECTION

As the ADR contains more than three PDs, we develop two methods to determine which PDs are selected to estimate the user position.

1) HIGHEST-POWER METHOD

The proposed ADR approach may lead to a large number of PDs receiving the signal retroreflected by the CCR. Specifically, the set of PDs that receive useful signals above a power threshold are grouped in a vector $\mathbf{p} = \{P_i \geq p_{\text{th}},\ i = 1, \ldots, I\}$. Then, the straightforward method is based on selecting the three PDs that receive the highest power. However, notice that this method may select the closest PDs in the ADR, which can be subject to high correlation responses. As a consequence, solving the positioning problem (see (18)) can be penalized because of the correlation among channel responses.

2) HIGHEST-VARIATION METHOD

To avoid selecting the three closest PDs of the ADR, a method based on selecting the channel response that provides the highest variation is proposed. First, the vector $\mathbf{p}$ is calculated to ensure channel responses above a threshold p_{th}. After that, the combination of three PDs from vector $\mathbf{p}$ that obtains the highest coefficient of variation denoted by CV is selected. It is worth noticing that CV is a statistical metric used to analyze the dispersion within a single dataset [31]. Specifically, for the considered problem, it is defined as

$$\text{CV} = \frac{\text{std}(\mathbf{P}_{\text{comb}})}{\text{mean}(\mathbf{P}_{\text{comb}})}, \tag{20}$$

where $\mathbf{P}_{\text{comb}}$ represents the vector containing a given combination of three power values. For configurations containing

multiple PDs, this approach ensures the selection of those with the least correlated channel responses. It reduces conflicts within the optimization problem that could arise from having highly similar power values and PD parameters.

The selected values of power with their corresponding PD parameters are used by the solver to estimate the position, as described previously in Section IV. Once the solver finds the estimated position of the user, the localization error is computed as

$$\Delta \mathbf{u} = \|\mathbf{u} - \hat{\mathbf{u}}_{\mathbf{opt}}\|, \tag{21}$$

which represents the absolute error measuring the Euclidean distance between the exact and the estimated position.

V. COMMUNICATION

An orthogonal approach between communication and positioning is assumed, e.g., time division multiplexing (TDM) performing uplink communication and positioning in different time slots. For enabling data transmission, an LC shutter is placed over the CCR acting as a modulator, which blocks or allows passing the reflected light by the CCR. Then, the PDs contained in the ADR receive the reflected signal and decode it for communication or positioning purposes. Consequently, the signal received at PD i because of transmission of user k is given by (4), recalling that transmission power and noise are detailed at the beginning of Section IV.

The concept of ADR can be inherently exploited for communication purposes. At this point, notice that this work is focused on positioning performance. Then, basic application of ADRs for communications will be analyzed. Specifically, the select best combining schemes (SBC) simply selects the PD that receives the strongest channel from user k. In this case, the spectral efficiency[3] is given by

$$\mathrm{SE}_{\mathrm{SBC},k} \leq \frac{1}{2}\log_2\left(1 + \frac{e}{2\pi}\frac{h_{\mathrm{SBC},k}^2 P_t}{\sum_{\substack{k'=1\\k'\neq k}}^{K} h_{\mathrm{SBC},k'}^2 P_t + \sigma^2}\right), \tag{22}$$

where $h_{\mathrm{SBC},k}$ is the channel at the PD selected for receiving the signal from user k. On the other hand, the equal gain combining (EGC) scheme selects all the PDs that compose the ADR for receiving the communication signal. Therefore, the spectral efficiency can be written as

$$\mathrm{SE}_{\mathrm{EGC},k} \leq \frac{1}{2}\log_2\left(1 + \frac{e}{2\pi}\frac{\sum_{i=1}^{I} h_{ik}^2 P_t}{\sum_{\substack{k'=1\\k'\neq k}}^{K}\sum_{i=1}^{I} h_{ik'}^2 P_t + \sigma^2}\right). \tag{23}$$

It is worth remarking that other schemes such as maximum ratio combining, optimum combining, or non orthogonal multiple access [19], [33] can be applied exploiting the concept of angular diversity.

Since this work considers the positioning footprint as the area in which the position of the users can be precisely determined, the average area spectral efficiency (AASE) is proposed for analyzing the communication performance. Specifically, it is calculated as,

$$\mathrm{AASE} \leq \frac{\frac{1}{N_u}\sum_{p=1}^{N_u}\mathrm{SE}_p}{A_\mathrm{c}}, \tag{24}$$

where N_u is the total number of instances of positions in which the scenario is divided, SE_p is the spectral efficiency of the communication scheme in position p, and A_c is the obtained positioning footprint, i.e., the area in which the positioning error is below a specific threshold.

VI. SIMULATION RESULTS

In this section, the performance of the proposed methods for positioning and communications is analyzed. The scenario corresponds to a square room whose dimensions are 4 m × 4 m × 3 m. The user is located in a random position among the X-Y plane and maintains a fixed position $d_z = 1$ m from the floor. The optical transmitter is a 40 × 40 cm LED panel providing an optical power equal to $P_\Sigma = 20$ W and it is assumed that the power is uniformly transmitted along the $J = 3200$ points that compose the LED panel. For a fair comparison of the simulation results, the same LED panel is assumed for both non-angular and angular approaches (centralized and decentralized configurations). The FoV of the PDs deployed along the LED panel is characterized by a wide FoV to guarantee overlapping among them, i.e., multiple PDs may receive the retroreflected signal. Specifically, we consider a FoV equal to 70°. All other parameters are listed in Table 1. Note that a high absolute temperature value of 370 K is considered in the PD due to the significant heat produced by a high-power LED during its operation. Moreover, we consider that the positioning footprint is defined as the area around the center of the scenario in which the positioning error is below 0.1 m. Focusing on the angular diversity arrangements deployed on the LED panel, the following configurations are considered

- *Non-angular*. The set of I PDs are pointing perpendicular downwards and the distance among PDs is S_{PD}. This configuration is denoted by $\mathrm{Non-angular}\,(I, S_{\mathrm{PD}})$, and it is considered as our baseline scheme [8].
- *Angular*. The set of I PDs are distributed following an angular diversity arrangement characterized by an elevation angle γ. The distance among PDs is given by S_{PD}. Moreover, the cases of centralized and decentralized schemes described in Fig. 5 and Fig. 6, respectively, are specifically considered. This configuration is denoted by $\mathrm{Angular}\,(I, S_{\mathrm{PD}}, \gamma)$.

A. BASELINE SCHEME VS. PROPOSED ANGULAR SCHEMES

The positioning accuracy for the baseline scheme [8] and the proposed solution for an elevation angle equal to $\gamma = 40°$ is depicted in Fig. 10. In this case, 5 PDs are deployed ensuring a separation distance of 20 cm among them. For the method based on selecting the PDs that receive the highest power, it can be seen that the footprint in which

[3]Unlike RF systems, optical intensity modulation and direct detection (IM/DD) data transmission cannot be bounded by the Shannon capacity. Then, we followed up with the tighter bound proposed in [32].

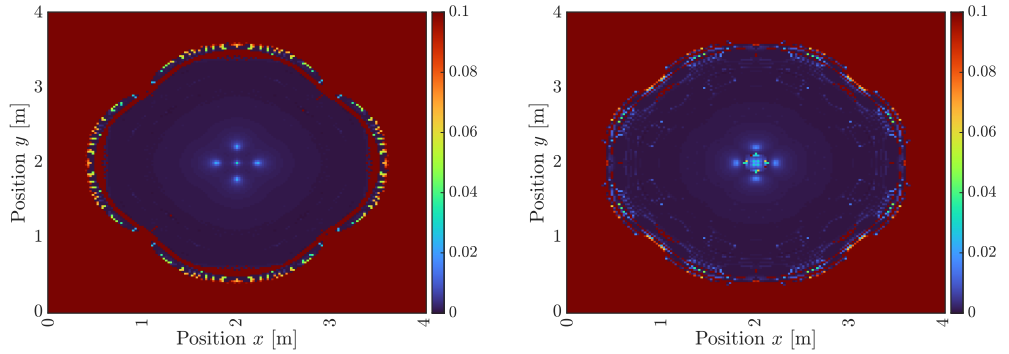

(a) Non − angular ($I = 5, S_{\mathrm{PD}} = 20\,\mathrm{cm}$). Highest-power method.

(b) Non − angular ($I = 5, S_{\mathrm{PD}} = 20\,\mathrm{cm}$). Highest-variation method.

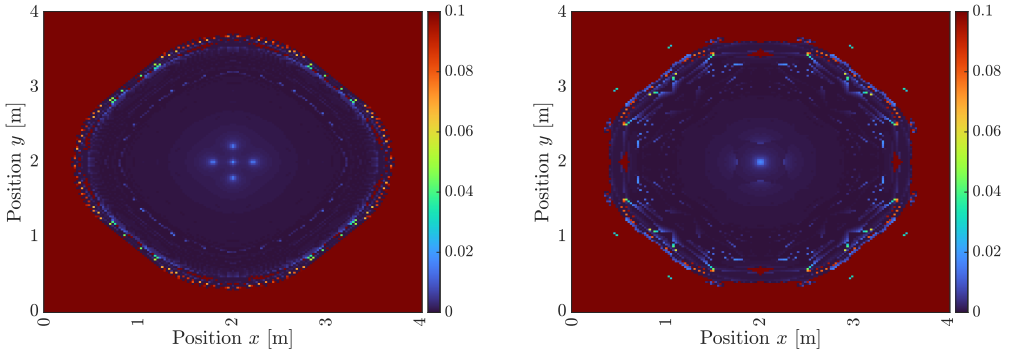

(c) Angular ($I = 5, S_{\mathrm{PD}} = 20\,\mathrm{cm}, \gamma = 40°$). Highest-power method.

(d) Angular ($I = 5, S_{\mathrm{PD}} = 20\,\mathrm{cm}, \gamma = 40°$). Highest-variation method.

FIGURE 10. Heatmap of the positioning error for $I = 5$ PDs and a distance between PDs equal to 20 cm. Non-angular approach and angular $\gamma = 40°$.

accurate positioning is achieved increases by exploiting the angular diversity. Specifically, the diameter of the footprint is increased by 21%, from a diameter of 2.8 m to 3.4 m, in the proposed scenario. On the other hand, for the highest variation method, it can be seen in Fig. 10(b) that this positioning footprint slightly increases by 12%. Furthermore, for both schemes, notice that some small areas (dots) in which the positioning error results high may appear. This is because of the correlation among the channel responses of the PDs.

To complete the comparison between the baseline and the proposed angular scheme, the mean positioning error is depicted in Fig. 13 as a function of the separation distance between PDs. For the non-angular approach, the positioning error decreases as the separation between PDs increases for values up to 20 cm. This is because separation among PDs is required to avoid high correlation of channel responses between neighboring positions. However, when the distance between PDs exceeds 30 cm, some PDs may not receive a useful signal, rendering the system incapable of resolving the position accurately. From now on, a non-angular configuration considering a separation distance between PDs equal to 20 cm is adopted as the baseline for comparison purposes. For the proposed angular approach, a lower positioning error is obtained within the range of 5 cm to 30 cm. Beyond this range, the angular approach is also subject to a lack of useful signals for resolving the positioning system. The proposed angular approach may solve this issue considering ADRs composed of a larger number of PDs.

The arrangement of PDs proposed to obtain the positioning footprints described in Fig. 10 requires large LED panels to exploit spatial diversity by maintaining a sufficient separation distance between the PDs. In Fig. 11 the positioning error is depicted to ensure the minimum distance among PDs in a centralized structure as described in Fig. 5. That is, by exploiting angular diversity alone (the distance between PDs can be considered negligible) the proposed centralized ADR can be integrated in a compact form, without the need for LED panels. In this case, the non-angular approach is subject to a poor accuracy and the positioning footprint comprises few centimeters. This effect is due to the correlation among the channel response of the PDs, i.e., all the PDs receive almost the same power. In contrast, exploiting the angular diversity leads to a considerable enhancement of the positioning coverage footprint. By selecting the PDs that receive the highest power, the positioning radius is about 3.65 m. Moreover, it can be seen that the positioning is degraded at the edge of this area. Although a similar positioning footprint is obtained for the highest variation method, it can be seen

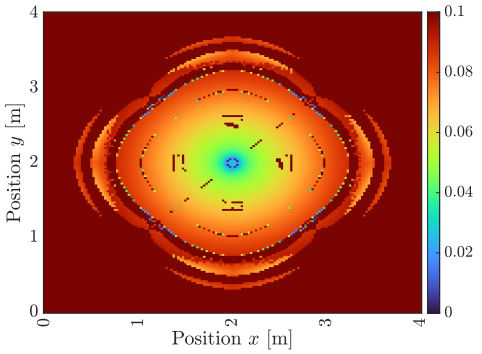

(a) Non − angular $(I = 5, \text{Centralized})$. Highest-power method.

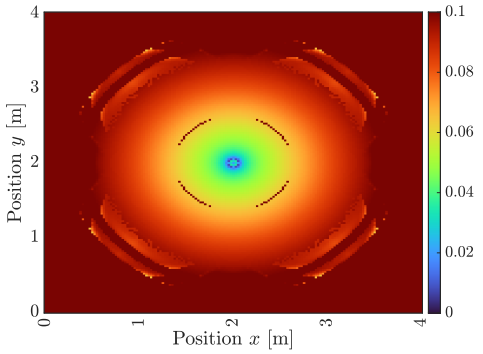

(b) Non − angular $(I = 5, \text{Centralized})$. Highest-variation method.

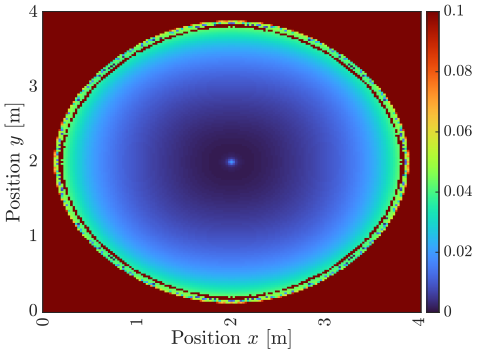

(c) Angular $(I = 5, \text{Centralized}, \gamma = 40°)$. Highest-power method.

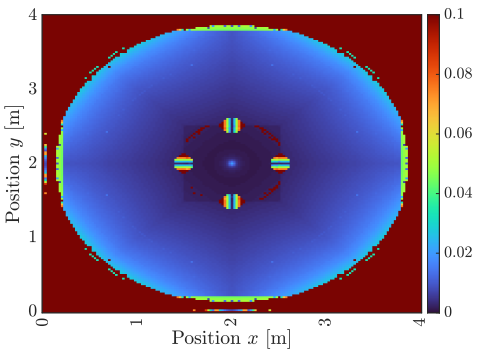

(d) Angular $(I = 5, \text{Centralized}, \gamma = 40°)$. Highest-variation method.

FIGURE 11. Heatmap of the positioning error for $I = 5$ PDs and a minimum distance among PDs (centralized structure). Non-angular approach and angular $\gamma = 40°$.

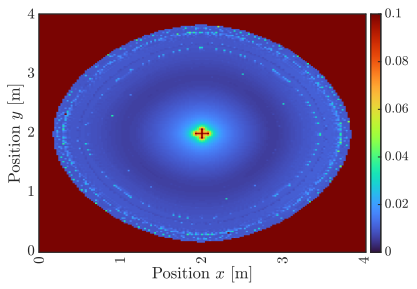

(a) Angular $(I = 5, \text{Decentralized}, \gamma = 40°)$. Highest-power method.

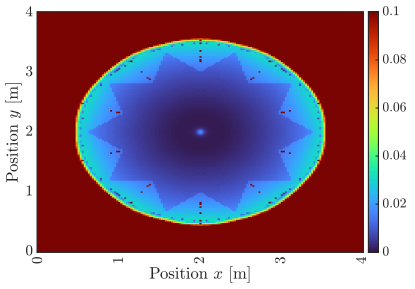

(b) Angular $(I = 11, \text{Decentralized}, \gamma = 40°)$. Highest-power method.

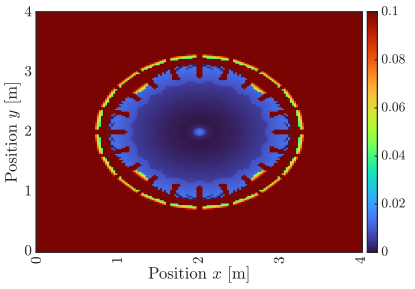

(c) Angular $(I = 21, \text{Decentralized}, \gamma = 40°)$. Highest-power method.

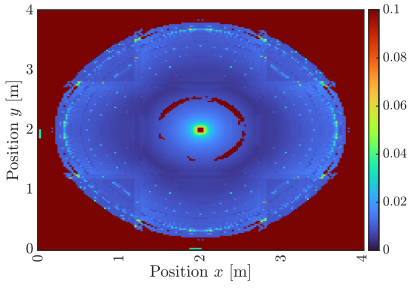

(d) Angular $(I = 5, \text{Decentralized})$. Highest-variation method.

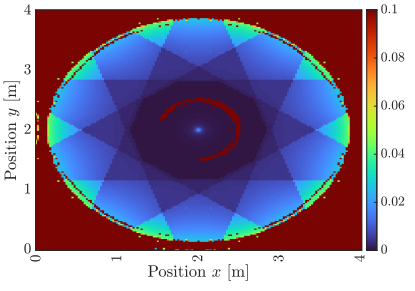

(e) Angular $(I = 11, \text{Decentralized}, \gamma = 40°)$. Highest-variation method.

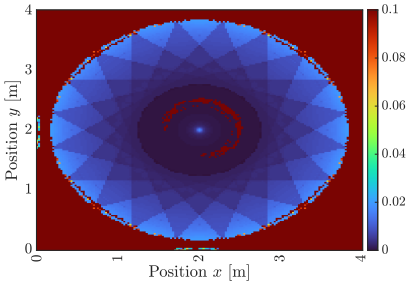

(f) Angular $(I = 21, \text{Decentralized}, \gamma = 40°)$. Highest-variation method.

FIGURE 12. Heatmap of the positioning error for $I = \{5, 11, 21\}$ PDs and a distance between PDs equal to the minimum among them. Angular deployment $\gamma = 40°$.

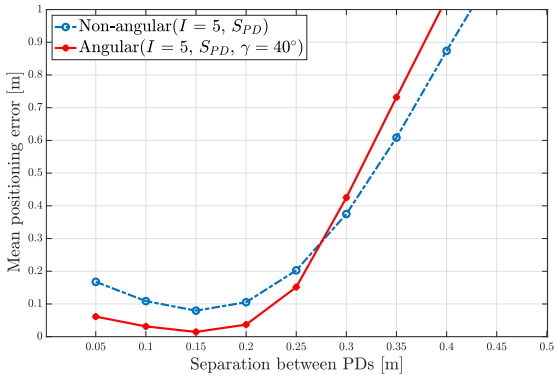

FIGURE 13. Separation between PDs vs. mean error in the positioning error.

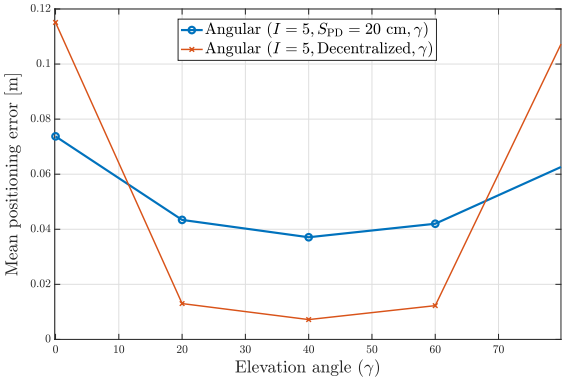

FIGURE 15. Average error vs. elevation angle for *I* = 5 PDs.

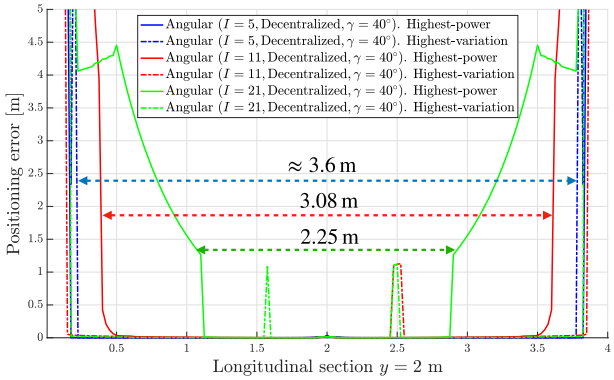

FIGURE 14. Longitudinal value of the positioning error in *x* axis at *y* = 2 m for the heatmaps shown in Fig. 12.

TABLE 1. Simulation parameters.

Average background noise power, $P_{\rm n}$ (W)	0.2
Bandwidth, B (Hz)	300×10^3
Refractive index of the CCR, η_1 η_2	1, 1.5
Transmitter semiangle, $\theta_{\frac{1}{2}}$ (degrees)	60°
Responsivity, ρ (A/W)	0.6
Reflecting loss factor, β	1
Load resistance, $R_{\rm L}$ (Ω)	50
Absolute temperature, $T_{\rm k}$ (K)	370

that the positioning is degraded in some specific areas of the scenario.

Focusing on angular diversity arrangements, the impact of the number of PDs is analyzed in Fig. 12. The distance among PDs is the minimum that ensures that no one falls into the ERA of other PDs following the decentralized ADR structure. Considering an ADR equipped with 5 PDs, it can be seen in Fig. 11(c) that the accuracy using the highest power method is penalized at the edge of positioning footprint. Then, other configurations composed of a larger number of PDs can be assumed with the aim of improving the accuracy. However, for a large number of PDs, the highest-power method likely selects neighboring PDs, which lead to correlated channel responses. It can be seen that indeed the diameter of the positioning footprint is reduced from 3.65 m to 3.1 m and 2.55 m for 11 and 21 PDs, respectively, for the highest-power method, seen in Fig. 12(b) and Fig. 12(c). Moreover, notice that some area is subject to a poor accuracy solving the positioning optimization problem due to the correlation among channel response. This issue can be potentially solved applying the highest-variation method. In this case, notice that the diameter of the positioning footprint is maintained as the number of PDs increases while removing the points where a poor accuracy is obtained (see Fig. 12(d), Fig. 12(e) and Fig. 12(f)). However, this method is subject to a lower accuracy than the highest power method in the inner cell.

The longitudinal section of the positioning error for y = 2 m in the heatmaps described in Fig. 12 are plotted in Fig. 14. It is worth remarking that positioning errors above 0.1 m for the previous heatmaps is given by the lack of three or more useful retroreflected signal at the ADR or the high correlation among them. The diameter of the positioning footprint can be easily determined, which values are summarized in Table. 2. Moreover, the impact of correlated responses at the inner cell for the highest-variation method can be also noticed.

When comparing both proposed angular structures, we observe the following results. The average error in the positioning footprint is analyzed in Fig. 15 as a function of the elevation angle assuming 5 PDs and both configurations; a separation between PDs equal to 20 cm and the minimum distance among them. It can be seen that lower average error is obtained for elevation angles between 20° and 60°. From now on, an elevation angle equal to 40° and a decentralized ADR is assumed, unless otherwise is specified. As expected, the average error increases when the elevation angle is zero, i.e., there is not angular diversity. Interestingly, the average error is much greater for non-angular diversity if the distance between PDs corresponds to the minimum since the channel responses are more correlated than assuming a distance between PDs of 20 cm.

B. PROPOSED MIXED HIGHEST -POWER AND -VARIATION POSITIONING METHODS

The results described above show a trade-off between the highest-power and highest-variation methods. At this point,

TABLE 2. Diameter of the positioning, footprint.

	$I = 5$ PDs Non-Angular	$I = 5$ PDs Centralized	$I = 5$ PDs Decentralized	$I = 11$ PDs Decentralized	$I = 21$ PDs Decentralized
Highest-power method	2.8 m	3.4 m	3.65 m	3.08 m	2.25 m
Highest-variation method	3 m	3.2 m	3.55 m	3.65 m	3.65 m
Mixed method	3 m	3.4 m	3.6 m	3.65 m	3.65 m

TABLE 3. Area spectral efficiency in bits/sec/Hz/m^2.

	$I = 5$ PDs Non-Angular	$I = 5$ PDs Decentralized	$I = 21$ PDs Decentralized
SBC	0.207	0.244	0.251
EGC	0.246	0.280	0.283

Algorithm 1 Pseudo-Code for Subroutine for Selecting the Received Power for Processing

Data: $\mathbf{P}$, P_{th}, CV_{th}
Result: $\hat{\mathbf{u}}$
$\mathbf{P} = P_i > P_{\text{th}}$
if $\mathbf{CV}(\mathbf{P}) \leq CV_{th}$ **then**
  $P_1, P_2, P_3 = \max(\mathbf{P})$
else
  $\mathbf{P}_{\text{comb}} = \binom{\mathbf{P}}{3}$
  $P_1, P_2, P_3 = \max(\mathbf{CV}(\mathbf{P}_{\text{comb}}))$
$\hat{\mathbf{u}} = \text{fsolve}(P_1, P_2, P_3)$

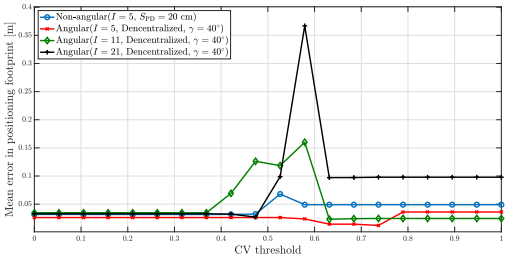

(a) Mean error given a threshold for the mixed positioning method.

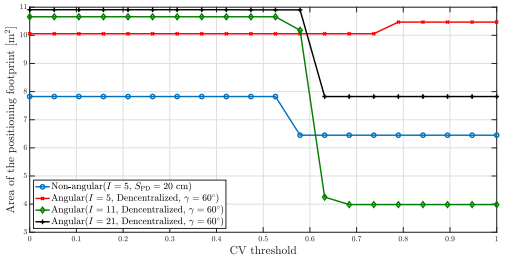

(b) Positioning area given a threshold for the mixed positioning method.

FIGURE 16. Analysis of the average error and area of the positioning footprint for the proposed mixed method.

we propose a CV threshold to define a criterion for applying a specific method. This procedure is described in **Algorithm** 1. The first step is to select the PDs that receive a useful signal above a threshold. This threshold, denoted by P_{th}, is selected according to the noise power. Specifically, a threshold twice the noise level is assumed to ensure that $\mathbf{P}$ contains useful signal retroreflected from the CCR. Additionally, the CV calculated as in (20) of the selected power values $\mathbf{P}$, is compared with a threshold denoted by CV_{th}. If the variability coefficient of $\mathbf{P}$ is below this threshold, highest-power method is chosen. On the other hand, if the variability of $\mathbf{P}$ is higher than the threshold, highest-variation method is chosen. The range of the threshold for the coefficient of variation goes from 0 to 1, and it is established based on the properties of this metric documented in the literature [31]. As extreme examples, the highest-variation method is always applied if $CV_{\text{th}} = 0$ while the highest-power method corresponds to $CV_{\text{th}} = 1$.

The impact of the CV threshold in both the average error within the positioning footprint and the area of this footprint are analyzed in Fig. 16 for different ADR configurations. As can be seen in Fig. 16(a), there is not a single optimum value of CV threshold, while the values between 0.35 and 0.65 should be avoided, specially, for arrangements composed of a large number of PDs. Furthermore, an average error below 5 cm can be seen within the positioning footprint for all the configurations. However, they have a direct impact on the area of the positioning footprint. In Fig. 16(b), it can be seen that exploiting the angular diversity leads to a considerable enhancement of area in which accurate position is obtained. Specifically, the positioning footprint increases from 7.82 m^2 to 10.05 m^2, 10.65 m^2 and 10.91 m^2 for 5, 11 and 21 PDs, respectively. It is worth noticing that the 5 PDs configuration improves the area by 28.5% exploiting diversity, while this improvement corresponds to 36.2% and 39.5% for increasing the number of PDs from 11 to 21.

According to the results obtained, a threshold $CV_{\text{th}} = 0.32$ is selected to calculate the positioning error for the considered angular configurations. For the sake of an easy explanation, we focus on the $I = 21$ PDs case, in which the difference between highest-power and highest-variation methods is more noticeable. Moreover, the error is evaluated for the elevation angles 40° and 60° in Fig. 17. First, it can be seen that the mixed method solves the reduction of the positioning area of highest-power method (see Fig. 12(c)). In this case, the sensing positioning diameter is equal to 3.65 m for both elevation angles of 40° and 60°, respectively. Although uniform positioning is obtained for an elevation equal to 40°, with an average error equal to 1.26 cm, the angular diversity is more noticeable for an elevation angle

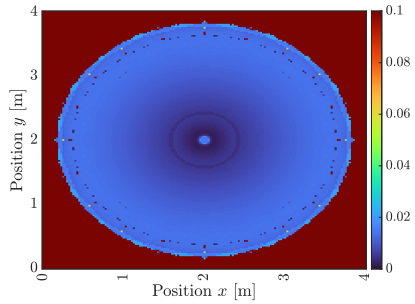

(a) Angular $(I = 21, \text{Decentralized}, \gamma = 40°)$. Mixed method $CV_{\text{th}} = 0.32$

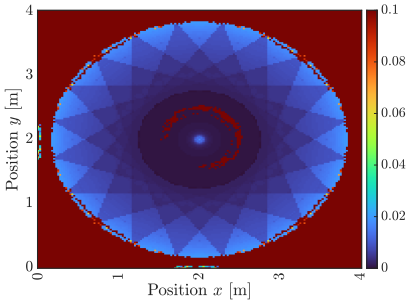

(b) Angular $(I = 21, \text{Decentralized}, \gamma = 60°)$. Mixed method $CV_{\text{th}} = 0.32$

FIGURE 17. Heatmap of the positioning error for the proposed mixed method. I = 21 PDs and a distance between PDs equal to the minimum among. Angular deployment $\gamma = \{40°, 60°\}$.

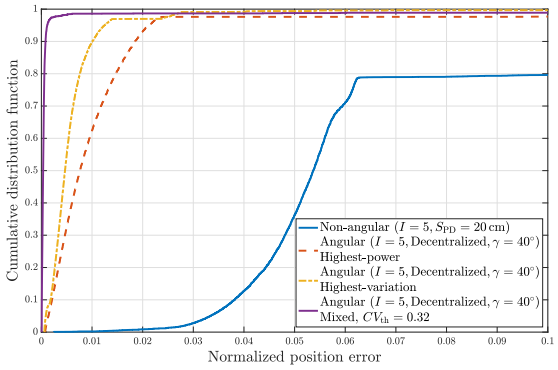

FIGURE 18. CDF of the normalized positioning error for a 5 PDs configuration.

of 60°. Specifically, lower positioning error can be achieved for this case. However, there exist some points around the inner cell where the error is high, greater than 1 m indeed, because of the lack of enough received signals with a high correlation among them.

To conclude the study of the positioning performance, the configuration composed on $I = 5$ PDs is analyzed considering the normalized position error, which is defined as the average error divided by the diameter of the positioning footprint, which is summarized in Table 2. The cumulative distribution function (CDF) of this parameter is plotted in Fig. 18. First, it can be seen that the baseline scheme non-exploiting the angular diversity is subject to higher normalized position

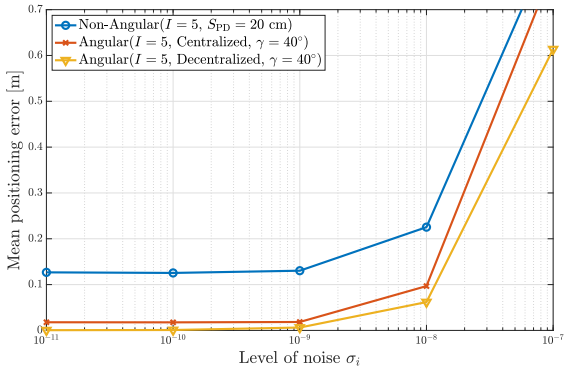

FIGURE 19. Mean positioning error vs. level of noise.

error than angular solutions. Specifically, an error greater than 5 cm is obtained in 60% of the positions. Moreover, extremely high error occurs in about 20% of the positions, greater than 1 m, which are not plotted in Fig. 18 for the sake of clarity. Focusing on the positioning performance obtained by the angular diversity approach, it can be seen that the highest-power and highest-variation methods achieve a normalized position error about 2 cm and 1 cm for 90% of the locations. Then, it can be seen that, properly combining both methods, the lack of accuracy in some specific locations can be solved, which lead to accurate positioning in 99% of the locations within the footprint.

The mean positioning error across the footprint for a wide range of noise levels is depicted in Fig. 19. Note that the noise comprises not only thermal and shot noise, but also not managed interference resulting from effects such as multi-path or uplink interference, which is treated as noise. It can be seen that the positioning error barely increases for noise standard deviations between $\sigma = 10^{-11}$ and $\sigma = 10^{-9}$, indicating the system is not limited by noise. However, the error increases slightly to mean values of 0.2 m and 0.1 m for the non-angular and angular approaches, respectively, at $\sigma = 10^{-8}$. Beyond this value, the noise level becomes comparable to the retroreflected signal, leading to high positioning errors. In such cases, interference management techniques, such as frequency division multiplexing based on color filtering [15] or non-orthogonal multiple access [19], could be applied to maintain positioning accuracy.

C. ANALYSIS OF COMMUNICATION RESULTS

In the following, we analyze the impact of deploying ADRs on the LED panel for uplink data transmission. To characterize the impact of exploiting the angular diversity, we consider a two users scenario, in which user 1 is located in the center of the cell, i.e., just below the LED panel, and a user 2 moving in a longitudinal manner along the scenarios. It can be seen in Fig. 20(a) that user 1 is limited by interference when user 2 is close to the inner cell. That is, the signal transmitted by both users is received in the same PDs of the ADR, leading to intra-user interference. Notice that interference management schemes such as orthogonal

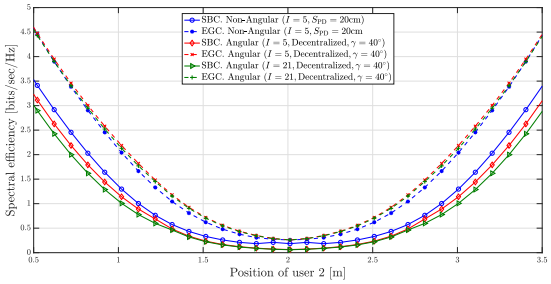

(a) Spectral efficiency of user 1 (cell center)

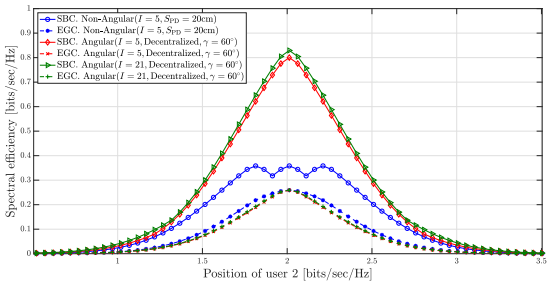

(b) Spectral efficiency of user 2 (longitudinal movement)

FIGURE 20. Spectral efficiency of a two-users scenarios. User 1 is located in a fixed position in the cell center while user 2 moves in a longitudinal manner along the scenario.

multiple access or non-orthogonal multiple access (NOMA) could be applied in this area. On the other hand, the rate of user 1 rapidly increases as user 2 moves out the inner cell. The impact of angular diversity in the uplink transmission is more noticeable for user 2 as shown in Fig. 20(b). First, it can be seen that EGC may increase the FoV of the receiver, but it does not manage the interference. On the other hand, SBC exploits the angular diversity, leading to higher spectral efficiency for user 2. At this point, it is worth noticing that other more complex ADR configurations such as hemispherical or multi-tier ADRs may improve the spectral efficiency.

Finally, the AASE is summarized in Table 3 for SBC and EGC schemes considering different ADR configurations. Notice that exploiting the angular diversity not only improves the size and accuracy of the positioning footprint but also increases the AASE within this footprint. Interestingly, it can be seen that a considerable enhancement of the AASE is obtained by exploiting the angular diversity for 5 PDs, i.e., the AASE increases by 17.8% and 13.8% for SBC and EGC, respectively. However, this enhancement is lower with the addition of more PDs. Specifically, increasing the number of PDs from 5 to 21, leads to an increase in the AASE of 2.9% and 1.07% for SBC and EGC, respectively. That is, greater rate enhancement is achieved by introducing angular diversity from a non-angular approach than increasing the number of PDs.

VII. CONCLUSION

In this work, angular diversity is proposed for passive positioning optical system based on retroreflecting the transmitted signal using CCRs. Typically, a large distance among PDs was assumed to avoid the correlation among the channel responses between close PDs, which limits positioning techniques to be used with large LED panels. By exploiting the angular diversity, this paper showed that accurate positioning can be achieved even for short separation distances among PDs, enabling the use of the proposed positioning scheme in small LEDs. Moreover, the error in positioning accuracy and, specially, the area in which this positioning is accurate are improved for the proposed scheme. It is demonstrated that defining a criterion for selecting PDs to perform positioning algorithms is required to avoid correlated channel responses as the number of PDs increases.

In a real-world system, the practicality of the proposed system is feasible as it consists of embedding several PDs in the LED panel, which may be implemented by lighting source manufacturers. Besides, as our proposal offers a good positioning performance with small PD separations, it enables its integration in realistic LED panels of a few cm^2, unlike the state of the art that requires large LED panels, whose size may not always be practical. Regarding the user device, we showed that commercial off-the-shelf CCRs can be used as we considered traditional CCR characteristics. Its geometry may influence the positioning and communication performance but, comparatively, our PD arrangement offers a better performance than the state of the art. This theoretical and simulation-based study opens the door to future experimental research that exploits the visible light for positioning and passive communication.

REFERENCES

[1] H. Haas et al., "Introduction to indoor networking concepts and challenges in LiFi," *J. Opt. Commun. Netw.*, vol. 12, no. 2, pp. A190–A203, Feb. 2020.
[2] Z. Zhu, Y. Yang, M. Chen, C. Guo, J. Cheng, and S. Cui, "A survey on indoor visible light positioning systems: Fundamentals, applications, and challenges," *IEEE Commun. Surveys Tuts.*, vol. 27, no. 3, pp. 1656–1686, Jun. 2025.
[3] M. Alijani, W. Joseph, and D. Plets, "Unmodulated visible-light positioning: A deep-dive into techniques, studies, and future prospects," *IEEE Open J. Commun. Soc.*, vol. 6, pp. 9448–9485, 2025.
[4] S. Shao et al., "An indoor hybrid WiFi-VLC internet access system," in *Proc. IEEE 11th Int. Conf. Mobile Ad Hoc Sensor Syst.*, Oct. 2014, pp. 569–574.
[5] T. Metin, M. Emmelmann, M. Corici, V. Jungnickel, C. Kottke, and M. Müller, "Integration of optical wireless communication with 5G systems," in *Proc. IEEE Globecom Workshops (GC Wkshps*, Dec. 2020, pp. 1–6.
[6] B. G. Guzman et al., "Toward sustainable greenhouses using battery-free LiFi-enabled Internet of Things," *IEEE Commun. Mag.*, vol. 61, no. 5, pp. 129–135, May 2023.
[7] M. S. Mir, B. G. Guzmán, A. Varshney, and D. Giustiniano, "LiFi for low-power and long-range RF backscatter," *IEEE/ACM Trans. Netw.*, vol. 32, no. 3, pp. 2237–2252, Dec. 2023.
[8] S. Shao, A. Salustri, A. Khreishah, C. Xu, and S. Ma, "R-VLCP: Channel modeling and simulation in retroreflective visible light communication and positioning systems," *IEEE Internet Things J.*, vol. 10, no. 13, pp. 11429–11439, Jul. 2023.
[9] Y. Wu, P. Wang, K. Xu, L. Feng, and C. Xu, "Turboboosting visible light backscatter communication," in *Proc. Annu. Conf. ACM Special Interest Group Data Commun. Appl., Technol., Architectures, Protocols Comput. Commun.*, Jul. 2020, pp. 186–197.
[10] X. Xu et al., "PassiveVLC: Enabling practical visible light backscatter communication for battery-free IoT applications," in *Proc. 23rd Annu. Int. Conf. Mobile Comput. Netw.*, 2017, pp. 180–192.

[11] P. Wang et al., "Renovating road signs for infrastructure-to-vehicle networking: A visible light backscatter communication and networking approach," in *Proc. 26th Annu. Int. Conf. Mobile Comput. Netw.*, Apr. 2020, pp. 1–13.
[12] T. Xu, M. C. Tapia, and M. Zúñiga, "Exploiting digital micro-mirror devices for ambient light communication," in *Proc. 19th USENIX Symp. Networked Syst. Design Implement. (NSDI 22)*, Apr. 2022, pp. 387–400.
[13] S. Shao, A. Khreishah, and H. Elgala, "Pixelated VLC-backscattering for self-charging indoor IoT devices," *IEEE Photon. Technol. Lett.*, vol. 29, no. 2, pp. 177–180, Jan. 15, 2017.
[14] L. De Groot, T. Xu, and M. Z. Zamalloa, "DroneVLC: Exploiting drones and VLC to gather data from batteryless sensors," in *Proc. IEEE Int. Conf. Pervasive Comput. Commun. (PerCom)*, Mar. 2023, pp. 242–251.
[15] S. Shao, A. Khreishah, and I. Khalil, "RETRO: Retroreflector based visible light indoor localization for real-time tracking of IoT devices," in *Proc. IEEE Conf. Comput. Commun.*, Apr. 2018, pp. 1025–1033.
[16] S. Shao, A. Khreishah, and I. Khalil, "Enabling real-time indoor tracking of IoT devices through visible light retroreflection," *IEEE Trans. Mobile Comput.*, vol. 19, no. 4, pp. 836–851, Apr. 2020.
[17] S. Shao, A. Salustri, A. Heusser, H. Khaniani, M. Hassanalian, and P. Roghanchi, "Downlink-uplink symmetry in mobile battery-free retro-reflective VLC: Enabling sensing-assisted communications," in *Proc. IEEE Int. Conf. Commun. Workshops (ICC Workshops)*, Jun. 2024, pp. 1061–1066.
[18] D. Bykhovsky and S. Arnon, "Multiple access resource allocation in visible light communication systems," *J. Lightw. Technol.*, vol. 32, no. 8, pp. 1594–1600, Apr. 8, 2014.
[19] A. G. A. Al-Sakkaf and M. Morales-Céspedes, "On the need of angle diversity receiver for downlink NOMA-based visible light communication systems," *IEEE Open J. Commun. Soc.*, vol. 6, pp. 6177–6193, 2025.
[20] M. Morales-Céspedes, H. Haas, and A. G. Armada, "Optimization of the receiving orientation angle for zero-forcing precoding in VLC," *IEEE Commun. Lett.*, vol. 25, no. 3, pp. 921–925, Mar. 2021.
[21] A. Petroni, G. Scarano, R. Cusani, and M. Biagi, "Modulation precoding for MISO visible light communications," *J. Lightw. Technol.*, vol. 39, no. 17, pp. 5439–5448, Sep. 1, 2021.
[22] A. Nuwanpriya, S.-W. Ho, and C. S. Chen, "Indoor MIMO visible light communications: Novel angle diversity receivers for mobile users," *IEEE J. Sel. Areas Commun.*, vol. 33, no. 9, pp. 1780–1792, Sep. 2015.
[23] M. Morales-Céspedes, M. Biagi, and A. G. Armada, "On the need for angular diversity receivers in spatial MIMO visible light communications," in *Proc. GLOBECOM - IEEE Global Commun. Conf.*, Dec. 2024, pp. 331–336.
[24] A. G. Al-Sakkaf and M. Morales-Céspedes, "Interference management for VLC indoor systems based on overlapping field-of-view angle diversity receivers," *IEEE Access*, vol. 12, pp. 51431–51449, 2024.
[25] A. Petroni and M. Biagi, "On the convenience of perfect channel knowledge for spatial equalization of correlated MIMO-VLC links: Is it really worth it?" *J. Lightw. Technol.*, vol. 40, no. 18, pp. 6101–6115, Sep. 15, 2022.
[26] A. Salustri. (2021). *RetroRay: Experimental Ray Tracer for Visual Light Communciations Research*. [Online]. Available: https://github.com/trilusa/RetroRay
[27] J. R. Barry and J. M. Kahn, "Link design for nondirected wireless infrared communications," *Appl. Opt.*, vol. 34, no. 19, p. 3764, Jul. 1995.
[28] Z. Yang, Z. Wang, J. Zhang, C. Huang, and Q. Zhang, "Wearables can afford: Light-weight indoor positioning with visible light," in *Proc. 13th Annu. Int. Conf. Mobile Syst., Appl., Services*, Jun. 2015, pp. 347–359.
[29] C. Mensing and S. Plass, "Positioning algorithms for cellular networks using TDOA," in *Proc. IEEE Int. Conf. Acoust. Speed Signal Process.*, vol. 4, May 2006, pp. IV-513–IV-516.
[30] S. P. Ahmadi, A. Hansson, and S. K. Pakazad, "Distributed localization using Levenberg–Marquardt algorithm," *EURASIP J. Adv. Signal Process.*, vol. 2021, no. 1, p. 74, Dec. 2021.
[31] C. E. Brown, "Coefficient of variation," in *Applied Multivariate Statistics in Geohydrology and Related Sciences*. Berlin, Germany: Springer, 1998, pp. 155–157.
[32] J.-B. Wang, Q.-S. Hu, J. Wang, M. Chen, and J.-Y. Wang, "Tight bounds on channel capacity for dimmable visible light communications," *J. Lightw. Technol.*, vol. 31, no. 23, pp. 3771–3779, Dec. 23, 2013.
[33] Z. Chen, D. A. Basnayaka, X. Wu, and H. Haas, "Interference mitigation for indoor optical attocell networks using an angle diversity receiver," *J. Lightw. Technol.*, vol. 36, no. 18, pp. 3866–3881, Sep. 15, 2018.

ALEJANDRO LÓPEZ BARRIOS (Student Member, IEEE) received the B.Sc. degree in telecommunications and electronics engineering from the Technological University of Havana José Antonio Echeverría (CUJAE), Cuba, in 2017, and the M.Sc. degree in advanced telecommunications technologies from the Universidad Carlos III de Madrid, Spain, in 2022. He is currently pursuing the Ph.D. degree with the Department of Signal Theory and Communications, Universidad Carlos III de Madrid, Leganés, Spain. His research interests include future wireless networks, visible light communications, interference management, and hardware implementations.

BORJA GENOVÉS GUZMÁN (Senior Member, IEEE) received the B.Sc. degree from the Universidad Carlos III de Madrid, Spain, in 2013, the double M.Sc. degree (Hons.) in electrical engineering from the Universidad Carlos III de Madrid, and the Institut Mines-Télécom, France, in 2015, and the Ph.D. degree from the Universidad Carlos III de Madrid, in 2019. He was a Post-Doctoral Researcher with the IMDEA Networks Institute, for three years. He was a Marie Skłodowska-Curie Actions Post-Doctoral Global Fellow with the University of Virginia, USA, for two years. He has carried out research stays with the University of Southampton, U.K., for three months, and The University of Edinburgh, U.K., for three months. He is currently a Ramón y Cajal Researcher with the Universidad Carlos III de Madrid. He has published over 50 peer-reviewed contributions. He also holds one granted patent. His research career has been supported by three regional, four national, and five European research projects, three of them as a principal investigator. He was a recipient of the Best Paper Award at IEEE GLOBECOM, in 2025. His research interests include visible light communication (also referred to as LiFi), the Internet of Things (IoT), and low-power wireless communications. He received the Extraordinary Ph.D. Award. He received the First Prize in Graduation National Awards by the Ministry of Education, Culture and Sports from Spain.

MÁXIMO MORALES-CÉSPEDES (Member, IEEE) received the B.Sc., M.Sc., and Ph.D. degrees from the Universidad Carlos III de Madrid, Spain, in 2010, 2012, and 2015, respectively, all in electrical engineering, with a specialization in multimedia and communications. From 2015 to 2017, he was a Post-Doctoral Fellow with the Institute of Information and Communication Technologies, Electronics and Applied Mathematics (ICTEAM), Universite Catholique de Louvain. He has been a Visiting Scholar with the University de California, Irvine, The University of Edinburgh, and the University of Linkoping. Currently, he is with the Department of Signal Theory and Communications, Universidad Carlos III de Madrid, Spain. He has participated in more than 16 national and international research projects, coordinating three of them, and contracts with the industry, all of them related to wireless communications. He has published more than 60 papers in international journals and conference proceedings. He holds one granted patent. His research interests include interference management, hardware implementations, MIMO techniques, and signal processing applied to wireless communications. He was a recipient of the Best Paper Award at IEEE GLOBECOM 2025. In 2012, he was a finalist of the IEEE Region 8 Student Paper Contest. He has participated in the organizing committee of IEEE WCNC 2027, IEEE Vehicular Technology Conference (VTC) Spring 2025, IEEE Meditcom 2024, and IEEE GLOBECOM 2021; and a TPC member of several IEEE conferences (VTC, GLOBECOM, ICC, and WCNC). He is serving in the editorial board for IEEE OPEN JOURNAL OF THE COMMUNICATIONS SOCIETY (Associate Editor) and IEEE COMMUNICATIONS LETTERS (an Associate Editor).